

E-147
REVISED

Exclusive Compton Scattering and
 π^0 Photo-Production on the Proton

CHARLES HYDE-WRIGHT,[†] JAMES BECK
University of Washington, Seattle WA 98195

PETER BOSTED,[†] RAY ARNOLD, STEVE ROCK, ZEN SZALATA, JOE WHITE,
The American University, Washington D.C.

FRANK DIETRICH, KARL VAN BIBBER,
Lawrence Livermore National Laboratory, Livermore CA 94550

KEITH GRIFFIOEN,
University of Pennsylvania, Philadelphia, PA 19104

WILLIAM BERTOZZI, SHALEV GILAD, DAN DALE,
Massachusetts Institute of Technology, Cambridge MA 02139

and

LINDA STUART
Stanford Linear Accelerator Center

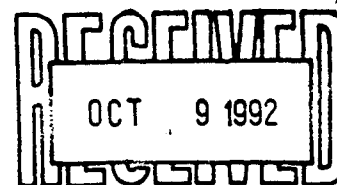
ABSTRACT

We propose to use a high flux bremsstrahlung beam in End Station A to measure the angular distribution of the exclusive $p(\gamma, \gamma p)$ and $p(\gamma, \pi^0 p)$ reactions at endpoint energies of 4, 6, 8.8, and 12.9 GeV. We will detect the recoil protons in the 8 GeV Spectrometer and the scattered photons in a Pb-Glass shower counter. These measurements will extend the present data to $s = 23 \text{ GeV}^2$ and $|t| = 13 \text{ GeV}^2$.

These are fundamental reactions that help reveal the short range structure of the proton. Dimensional counting predicts that at high energy and high momentum transfer, the $p(\gamma, \gamma p)$ and $p(\gamma, \pi^0 p)$ cross sections follow scaling laws $d\sigma(\gamma, \gamma')/dt = s^{-6} f_\gamma(\cos \theta_{CM})$, $d\sigma(\gamma, \pi^0)/dt = s^{-7} f_{\pi^0}(\cos \theta_{CM})$, respectively. There exist QCD predictions of $f_\gamma(\cos \theta_{CM})$ based on convoluting the minimal set of perturbative diagrams with the minimal Fock space proton distribution amplitude, extracted from QCD sum-rule analyses.

Submitted to *SLAC EPAC*

[†] Co-Spokesman



1. Introduction

Elastic photon scattering from the proton is a second order electromagnetic probe of the proton structure. At low energies (*i.e.* well below the Δ -resonance) recent measurements have determined the electric and magnetic polarizabilities of the proton.¹ At high energies and forward angles the cross section is most naturally discussed in terms of dispersion relations and the vector meson structure of the photon (*e.g.* Ref. 2). At high energy *and* high momentum transfer, the Compton cross section is sensitive to the short range structure of the proton. Thus the physics of Compton scattering, in this limit, is closely related to the high Q^2 measurements of the elastic form factors of the proton: G_E and G_M . Compton scattering is also closely related to the idea of Color Transparency, which posits the formation of a small three quark object in any high-momentum transfer semi-exclusive reaction on nuclei.³ We will use perturbative QCD (pQCD) as a framework for discussing Compton scattering, although we believe the justification for the present experimental proposal is more general than the specific issue of the present status of pQCD.

The internal momenta of the constituents of a hadron are soft (of order the proton mass M). It is natural to expect that in any high momentum transfer exclusive reaction, the momentum transfer will be shared amongst *all* of the constituents in the final state by the (perturbative) exchange of at least one hard gluon to each constituent. Each hard gluon exchange introduces a factor of order $1/t$ into the amplitude, where t is the invariant momentum transfer. We expect that to order M^2/t (equivalently M^2/s) the amplitude will be dominated by the simplest possible diagrams *i.e.* diagrams with the minimum number of soft constituents in the initial and final states (simplest Fock space configurations) and the minimum number of gluon exchanges, consistent with at least one hard gluon exchange to each soft constituent (quark, anti-quark, or gluon). These arguments lead naturally to the dimensional counting scaling law: In any exclusive reaction, at sufficiently high energy at a fixed center-of-mass scattering angle, the cross section scales as:⁴

$$\frac{d\sigma_x}{dt} = s^{2-n} f_x(\cos\theta_{CM}) \quad s \gg M^2, \quad (1.1)$$

where s is the total invariant mass squared and n is the minimum number of external fundamental fields in the invariant amplitude. For elastic Compton scattering on the proton, $n = 8$ (three quarks and a photon in the initial and final states). For the $p(\gamma, \pi^0)p$ cross section $n = 9$, thus the π^0 cross section should decrease more rapidly with s than the Compton cross section.

Fig. 1 displays the world's supply of high energy Compton data on the proton, plotted as $s^6 d\sigma/dt$ vs. $\cos\theta_{CM}$, to illustrate the approach to the asymptotic scaling law. There is a general envelope suggesting a universal $f(\cos\theta_{cm})$. However, in the forward direction the spread in the data as a function of s is nearly plus or minus one order of magnitude. Even at $\theta_{CM} = 60^\circ$, the total spread of the data is one order of magnitude. The pQCD scaling law is only an asymptotic prediction at large s and t . Fig. 2 restricts the data set to $t > 1.0$ (GeV/c)². Only one experiment remains, that of M.A. Shupe *et al.*, from Cornell.⁹ The scaling behavior of the Compton data is illustrated in Fig. 3. The most stringent test of the scaling law is obtained at $\theta_{CM} = 90^\circ$. Fitting the data to a $s^{-\alpha}$ power law, results in $\alpha = 7.0 \pm 0.4$: a 2.5σ deviation from the prediction of $\alpha = 6.0$. Fig. 4 displays the coherent π^0 production data obtained in the same experiment as the Compton data of Fig. 2. Again, the data are falling faster than the dimensional counting scaling law, except at $\theta_{CM} = 45^\circ$ where the data fall more slowly with s than the prediction.

Before discussing the feasibility of a new experiment on Compton scattering, we note that there is more to pQCD than the scaling laws. There exist "parameter-free" calculations of high energy proton Compton scattering.^{11,12} These calculations keep only the lowest order Feynman diagrams (there are 336 non-vanishing topologically distinct ways to couple two photons to three quarks with the exchange of two gluons) integrated over the proton distribution amplitude. In the high energy limit, the proton wave function (for the 3-quark Fock state) reduces to the distribution amplitude $\phi(x_1, x_2, x_3)$ of the momentum fractions $\{x_i\}$ of the three valence quarks, with the constraint $x_1 + x_2 + x_3 = 1$. The distribution amplitude is evaluated with QCD sum-rules. By convention, $\phi(x_1, x_2, x_3)$ is the amplitude for the Fock space configuration $|u_+(x_1)u_-(x_2)d_+(x_3)\rangle$, with the \pm subscripts identifying the quark helicity parallel or anti-parallel to the proton helicity. The amplitudes for the other spin-flavor configurations with the same momentum fractions are obtained from symmetry relations.¹² At sufficiently high momentum transfer, the distribution amplitude has the asymptotic form $\phi_{as}(\{x_i\}) = 120x_1x_2x_3$. However, "The asymptotic distribution function ... is as apt at present energies as the asymptotic δ -function structure function."¹² In the QCD sum-rule approach, $\phi(\{x_i\})$ is expanded in terms of ϕ_{as} times a polynomial in x_1, x_2, x_3 . In the present state of the art, the expansion of ϕ is truncated after the first six polynomial terms. The distributions from three commonly used different versions of the monomial expansion of ϕ are plotted in Fig. 5. In each case the distribution favors an up-quark with helicity parallel to the proton helicity carrying the dominant momentum fraction.

The pQCD calculations of Kronfeld and Nizic for the four different versions of the distribution amplitude in Fig. 5 are shown in Fig. 2 and in Fig. 3. Several

features are clear. First, there is wide disagreement amongst the theorists over the correct distribution amplitude. Second, the large variations in ϕ result in large variations in the predicted Compton cross section. Finally, none of the curves is in agreement with all of the data.

Clearly, new high precision data at large s will provide a powerful test of the scaling law (Eq. (1.1)) and the QCD sum rule distribution amplitude. Conversely, new Compton data can provide tighter constraints on the proton distribution amplitude of Fig. 5 then are presently obtained from QCD sum rules.

2. Experimental Proposal

We propose to use a high flux bremsstrahlung photon beam to measure proton Compton scattering; $p(\gamma, p\gamma)$ and exclusive π^0 photoproduction $p(\gamma, p\gamma)\gamma$ in End Station A. Compton events are defined by a coincidence of the scattered photon (energy k') in a Pb-Glass shower counter and the recoil proton in the 8 GeV Spectrometer. The proton recoil three-momentum \mathbf{p}_p defines the incident photon energy (k) for each Compton event. The γ -ray coincidence with the proton eliminates most of the real and accidental coincidences that compete with the Compton process.

Our proposed kinematics are listed in Table 1. This specific choice is described in Appendix A. The proposed kinematics are plotted in the t vs. s plane in Fig. 6 and the proton recoil angle θ_p vs. photon scattering angle θ_γ plane in Fig. 7. Fig. 6 also shows that these measurements will be the first data in the range $s > 12 \text{ GeV}^2$ and $t > 3 \text{ GeV}^2$. The expected results for Compton scattering are contrasted with the existing data and theories in Fig. 3.

The electron beam will be incident on a 6% radiator upstream of the target, and then dumped to minimize extraneous background in the End Station. The bremsstrahlung beam will be collimated to a 1.25 cm radius on the target. This spot size is constrained by resolution requirements, discussed below. With such small angular collimation, the photon flux on target is limited by multiple scattering. Using a gaussian estimate for the distribution of multiple scattering into angles smaller than the collimation angle θ_C we obtain a photon flux on target of

$$\begin{aligned} \frac{d\Phi_\gamma}{dk} &\approx \frac{I X_{\text{eff}}}{e k} \\ X_{\text{eff}} &= X \left[1 - \exp \left\{ - \left(\frac{k\theta_C}{21\text{MeV}} \right)^2 \frac{1}{X} \right\} \right] \\ &\lesssim \left(\frac{k\theta_C}{21\text{MeV}/c} \right)^2 \end{aligned} \quad (2.1)$$

where I/e is the incident electron flux and X is the radiator thickness in radiation lengths. For our count rate estimates, we have assumed the radiator is 50 m upstream of the target, or $\theta_C = 12.5 \text{ mm} / 50 \text{ m}$. At 12.9 GeV, the effective radiator thickness is approximately 2%, yielding an instantaneous photon flux on target within 10% of the endpoint of $8 \cdot 10^8 / \text{burst}$, or an average flux of $6 \cdot 10^{10}$ Hz with a beam rep. rate of 120 Hz and an electron beam flux of $5 \cdot 10^{11} / \text{burst}$. The photon beam will be monitored downstream of the target either with the quantameter used in the low- t experiment of Anderson^{5,13}, or with a device of similar design.

For convenience, we also define the integrated photon flux in equivalent quanta and the integrated photon luminosity:

$$\begin{aligned}\Phi_\gamma &= \int \frac{d\Phi_\gamma}{dk} k dk = \frac{I}{e} X_{\text{eff}} \\ \mathcal{L}_\gamma &= T \Phi_\gamma,\end{aligned}\tag{2.2}$$

where T is the target thickness (nucleons/cm²).

2.1 PROTON DETECTION

The 8 GeV Spectrometer will be operated in the high acceptance mode, with the field in quadrupoles Q81 and Q82 reversed such that the acceptance as a function of the proton recoil momentum p_p is:

$$\begin{aligned}\Delta\Omega &= 3.2\text{msr} & p_p \leq 4.5\text{GeV}/c \\ &= 3.2\text{msr} \cdot \left[\frac{4.5\text{GeV}/c}{p_p} \right]^2 & p_p > 4.5\text{GeV}/c\end{aligned}\tag{2.3}$$

For $p_p < 4.5 \text{ GeV}/c$, the acceptance is $\pm 20 \text{ mr}$ in the horizontal (scattering) plane and $\pm 40 \text{ mr}$ in the vertical (dispersion) plane. We will use an extended target of liquid H₂. In the new tune, the 8 GeV acceptance is flat only for a target length of $\pm 5 \text{ cm}$ in y (the horizontal coordinate perpendicular to the spectrometer axis), though the integrated relative acceptance is 80% for a target length of 20 cm (in y). Our count rate estimates are based on a target thickness of $2 \text{ g}/\text{cm}^2$ ($\approx 30 \text{ cm LH}_2$). For the spectrometer, this is a target length of $\Delta y = (30 \text{ cm}) \cdot \sin \theta_p$. In fact, it may be possible to use a longer target at the high- t points since as $-t$ increases, θ_p decreases (Fig. 7). The momentum acceptance of the 8 GeV Spectrometer will be tuned to the proton endpoint corresponding to the photon endpoint. We will accept protons within 5% of the endpoint in the spectrometer. Although a wider acceptance is possible, it brings additional proton singles rate from exclusive ρ production.

We plan to use the same detectors in the 8 GeV focal plane as were used in NE18, the last experiment to use this spectrometer. This experiment covered the same proton momentum range as the present experiment, and had similar background particle rates. Three planes of scintillators provide proton/pion separation by time-of-flight up to about 2.5 GeV/c. Above this, the gas Cerenkov counter takes over, firing for pions but not for protons. Ten planes of MWPC's will be used for tracking. A segmented hodoscope after the wire chambers helps to resolve track ambiguities when the rates are high. All the required electronics for these detectors exists in Counting House A (CHA).

Events will be defined by valid proton triggers in the 8 GeV spectrometer. For each proton event, we will record all photon hits in the calorimeter. For most of our kinematics, the 8 GeV Spectrometer acceptance is either at or below the the $p(\gamma, \pi^+)n$ endpoint. We have estimated the $p(\gamma, \pi^+)X$ rate in the 8 GeV Spectrometer. For all of the kinematics that we consider, this rate is less than the $p(\gamma, p)\pi^0$ rate, so the event rate will always be much less than one per pulse.

2.2 PHOTON DETECTION

The scattered photon will be detected in a calorimeter made out of at least 500 6.2 cm \times 6.2 cm \times 75 cm Pb-Glass blocks for a total of 2 m². Four hundred of these blocks (200 in each arm) are currently being used in experiment E142. They have been carefully refurbished, gain matched, and installed in boxes. We will build a new frame to house the entire assembly. The signals from the counters will go to CHA on fast foam cables. In CHA, a splitter box built at Saclay splits the signal five ways. One of these gets fanned together to make a total shower pulse height. Three of the remaining signals will go to ADCs (also currently in use for E142). Although only one ADC channel per block is required, the splitter permits us to integrate the pulse with three separate gates: a on-time narrow gate (30 ns), a on-time wide gate (80 ns), and an early gate. The narrow gate is optimized to minimize pile-up background at some cost in resolution. The wide gate will provide optimal resolution in those kinematics where the pile-up is negligible, and the early gate measures the random pile-up background. Finally, the last split-off signal will go to ECL discriminators and TDC's. The existing TDCs allow up to 16 hits per beam spill. The TDC's will allow us to make double arm time-of-flight measurements to reduce accidental coincidences.

To maximize the count rate, the calorimeter must be large enough to match the acceptance of the proton arm. In the vertical plane, the photon acceptance required is

$$\Delta\phi_\gamma = \frac{\sin\theta_\gamma}{\sin\theta_p} \Delta\phi_p = \pm \frac{\sin\theta_\gamma}{\sin\theta_p} 40 \text{ mrad} \quad (2.4)$$

This relation follows from the co-planarity condition on the proton and photon. Since large photon angles θ_γ are correlated with small recoil proton angles θ_p in Table 1, the vertical acceptance $\Delta\phi_\gamma$ required grows very large at large scattering angles. The horizontal acceptance $\Delta\theta_\gamma$ is discussed in Appendix B, at large photon angles, the horizontal acceptance has the same form as Eq. (2.4). Thus the optimal geometry for the 500 blocks is a rectangle 1 m wide by 2 m high. Furthermore, to optimize resolution and minimize background pile-up, at each angle the calorimeter should be placed as far from the target as possible, consistent with full Compton photon acceptance. One solution is illustrated in Fig. 8, The flight path $r_{EM}(\theta_\gamma)$ from target to calorimeter lies on a logarithmic spiral:

$$r_{EM}(\theta_\gamma) = r_0 \exp\left(\frac{\theta_0 - \theta_\gamma}{\tan \alpha}\right), \quad (2.5)$$

with $\theta_0 = 36^\circ$, $r_0 = 11$ m, and $\alpha = 15.9^\circ$. The calorimeter can be either moved by crane, or installed on a cart moving on rails. The logarithmic spiral insures that as the cart rolls along the rails, the calorimeter always points to the target.

Also sketched in Fig 8 is a sweeping magnet, to magnetically shield the calorimeter from charged particles from the target. This can be a standard 18D70 magnet with a 9 inch gap, oriented with the magnetic field horizontal so that the aperture matches the calorimeter acceptance. The magnet must be close to the target at large angles to match the calorimeter solid angle, but sufficiently far from the target at small angles that it does not interfere with the beam line. This can be accomplished by placing the midpoint of the magnet on a spiral defined by:

$$r_{18D70} = r_1 \exp\left(\frac{\theta_0 - \theta_\gamma}{\tan \alpha}\right) \quad (2.6)$$

with $r_1 = 5.07$ m and $\alpha = 20.23^\circ$.

We use a Pb-Glass calorimeter, rather than alternatives based on scintillators or wire chambers to minimize sensitivity to hadronic background (which does not produce Cerenkov radiation). To minimize background, we will also surround the calorimeter at each position with concrete shielding.

The energy resolution of the calorimeter blocks was recently measured at CERN to be

$$\frac{\sigma_E}{E} = \frac{10 - 11\%}{\sqrt{E}}. \quad (2.7)$$

This resolution will be degraded by several effects described below. We note, however, that Compton events will be identified by angular kinematics alone. The energy resolution of the calorimeter is only required to set a threshold to

separate exclusive events from the background of random coincidences of protons with inclusive $p(\gamma, \gamma')X$ events. The shower from a high energy photon can spread over several adjacent blocks. Our threshold will be set in software to require the sum of any four adjacent blocks to exceed approximately 30% of the Compton endpoint energy. This insures high acceptance for both Compton and exclusive π^0 photons.

2.3 $p(\gamma, \gamma'p)$ AND $p(\gamma, \pi^0p)$ RATES

The count rate is defined by:

$$\begin{aligned} \text{Rate} &= T \int \frac{d\phi_\gamma}{dk} dk \int \frac{d\sigma(\gamma, \gamma)}{d\Omega_\gamma} d\Omega_\gamma \\ &\approx \mathcal{L}_\gamma \frac{\Delta k}{k} \frac{d\sigma(\gamma, \gamma)}{d\Omega_\gamma} \Delta\Omega_\gamma \end{aligned} \quad (2.8)$$

However, the acceptance (both in momentum and solid angle) is defined by the proton arm. Thus

$$\text{Rate} \approx \frac{\mathcal{L}_\gamma}{k} \frac{d\sigma(\gamma, \gamma)}{d\Omega_\gamma} \Delta p_p \Delta\Omega_p \left/ \left| \frac{\partial(p_p, \cos \theta_p)}{\partial(k, \cos \theta_\gamma)} \right| \right. \quad (2.9)$$

We estimate in Table 1 and Fig.3 the Compton and coherent π^0 cross sections by extrapolating global fits to the data of Ref. 9 to higher s , assuming the s^{-6} and s^{-7} dimensional scaling laws, respectively, are valid.

The $p(\gamma, \gamma'p)$ and $p(\gamma, \pi^0p)$ reactions must be separated to identify each process. Both produce real coincidences between a proton and at least one photon. The difficulty in separating the processes is that the Compton cross section is 10 to 50 times smaller than the exclusive π^0 cross section. Because of the small mass of the pion, the four-momentum of a coherent π^0 is nearly identical to the four-momentum of a Compton photon, and the recoil proton four-momenta for Compton and coherent π^0 events are not resolvable. The energy of the Compton scattered photon is

$$k' = k / [1 + \frac{k}{M}(1 - \cos \theta_\gamma)]. \quad (2.10)$$

The π^0 decays into two photons with the leading photon of energy $E_\pi/2 \leq k_1 < E_\pi = k'$ in a cone (in the laboratory) of half angle $\theta_1 \leq m_\pi/E_\pi$. The second photon has energy $k_2 < E_\pi/2$ and lies outside the cone $\theta_2 = m_\pi/E_\pi$. In contrast, (for fixed proton kinematics) the Compton photon is spread out in solid angle only by the overall coincidence angular resolution. This resolution is discussed

in Appendix B. The ratio of the Compton photons to coherent π^0 photons is determined by the ratio of cross sections divided by the fraction of the π^0 photons falling within the Compton angular resolution. The angular resolutions in the scattering plane and out of the scattering plane are σ_θ and σ_ϕ , respectively. The 1σ spread in angles fills a solid angle $\Delta\Omega$. The fraction of the leading coherent π^0 decay photons within the solid angle $\Delta\Omega$ is

$$\begin{aligned}\pi^0 \text{ decay fraction} &= \frac{\Delta\Omega}{2\pi} \left. \frac{\partial \cos \alpha_{CM}}{\partial \cos \alpha_{lab}} \right|_{\theta_{lab}=0} \\ &= 2\sigma_\theta\sigma_\phi(E_\pi/m_\pi)^2.\end{aligned}\tag{2.11}$$

In Eq. (2.11), α_{CM} and α_{lab} is the angle of the π^0 decay photon in the π^0 rest-frame or lab-frame, respectively, relative to the momentum direction of the π^0 in the lab. Thus the ratio of Compton to π^0 photons within the Compton angular resolution is

$$\frac{\text{Compton Events}}{\pi^0 \rightarrow \gamma\gamma \text{ Events}} = \frac{d\sigma(\gamma, \gamma')}{d\sigma(\gamma, \pi^0)} \frac{63\%}{2} \frac{m_\pi/k'}{\sigma_\theta} \frac{m_\pi/k'}{\sigma_\phi},\tag{2.12}$$

where $63\% = 1 - \exp(-1)$ is the area within 1σ of a two-dimensional gaussian distribution. Eq. (2.12) is the signal to noise ratio listed in Column 4 of Table 2. An example of the experimental separation of Compton and exclusive π^0 production is shown in Fig. 9. We feel that our Compton to π^0 ratios are conservative, since the data at lower s show a ratio $d\sigma(\gamma, \gamma')/d\sigma(\gamma, \pi^0) \propto s^{2.0 \pm 0.3}$ rather than $s^{1.0}$ we assume in our estimates.

The calorimeter is optimized for \approx full acceptance of Compton photons. In general, we will not be able to detect both photons from exclusive π^0 decay. However, since the angular distribution of the leading photon from π^0 decay is determined by the Jacobian of Eq. (2.11), the coherent π^0 production cross section $p(\gamma, \pi^0 p)$ can be extracted with high precision from the co-planarity distribution (Fig. 9) of $p(\gamma, \gamma_1 p)\gamma_2$ events (in which the second photon is not detected). The angular spread m_π/E_π of the leading photons from exclusive π^0 decay is comparable to the calorimeter acceptance. Thus the experimental acceptance for $p(\gamma, \gamma_1 p)\gamma_2$ events is less than unity, but never less than 25%. Hence we will always have much higher statistics on exclusive π^0 production than on Compton scattering.

2.4 ATOMIC COMPTON SCATTERING

There is a potentially serious background in the calorimeter from the pile-up of low energy photons from Compton scattering from the atomic electrons in the target. As a function of photon angle these Compton photons have an energy

$$k' = \frac{m_e}{m_e/k + 1 - \cos \theta_\gamma} \approx \frac{m_e}{1 - \cos \theta_\gamma}. \quad (2.13)$$

At 15° , this energy is 15 MeV. The differential cross section is:

$$\frac{d\sigma(e + \gamma \rightarrow e + \gamma)}{d\Omega_{\text{lab}}} = \frac{\alpha^2}{2m_e^2} \left(\frac{k'}{k}\right)^2 \left[\frac{k}{k'} + \frac{k'}{k} - \sin^2 \theta_\gamma\right]. \quad (2.14)$$

After integrating over the photon flux, we obtain the mean energy deposited in a calorimeter block of solid angle $\Delta\Omega$ integrated over the ADC gate width Δt :

$$\langle E \rangle = \int \mathcal{L}_\gamma \frac{dk}{k} k' \frac{d\sigma}{d\Omega} \Delta\Omega \Delta t = \mathcal{L}_\gamma \frac{\alpha^2}{2m_e} \frac{5 + 3 \cos^2 \theta}{6(1 - \cos \theta)} \Delta\Omega \Delta t. \quad (2.15)$$

The only energy dependence in Eq. (2.15) is contained in the photon collimation in the photon luminosity \mathcal{L}_γ (Table 1). For a 1% effective radiator, the mean pile-up of Compton photons from atomic electrons varies with angle from 1 to 2 GeV, integrated over a 30 ns ADC gate and summed over four calorimeter blocks located on the logarithmic spiral of Eq. (2.5). The actual pile-up will be less than 1 GeV for most kinematics, in proportion to effective radiator thickness (Table. 1). The fluctuations in this pile-up will be small, since it is the sum of over 100 low energy photons. Following the example of Ref. 5, we will put a carbon absorber of up to 3 radiation lengths in front of our calorimeter in order to absorb most of these photons. This will degrade our energy resolution for high energy photons, as a result of the fluctuations in shower energy deposited in the absorber. With the absorber, the pile-up summed over four calorimeter blocks is easily reduced to less than 5% of the proton-Compton energy. At this level, this DC background is not a major factor.

2.5 ACCIDENTAL COINCIDENCE BACKGROUNDS

In addition to true gamma-proton coincidences from Compton scattering and π^0 production, we will also face a background of inclusive $p(\gamma, p)X$ triggers in the 8 GeV Spectrometer in accidental coincidence with inclusive $(\gamma, \gamma')X$ photons in the calorimeter. The proton acceptance will integrate over the $p(\gamma, p)\gamma$, $p(\gamma, p)\pi^0$, and $p(\gamma, p)X$ reactions up to a missing mass m_X at or near the ρ -meson. The SLAC measurements by Anderson¹⁵ of the $p(\gamma, p)X$ yield at $t \approx 1$ GeV and $k = 11.5$ GeV show that the integrated $p(\gamma, p)\pi\pi$ yield below ρ -threshold is approximately equal to the $p(\gamma, p)\pi^0$ yield. For the purposes of calculating accidental coincidence rates, we assume that the integrated $p(\gamma, p)X$ rate is equal to the $p(\gamma, p)\pi^0$ rate. On the calorimeter side, there is a large flux of inclusive photons, mostly from inclusive π^0 production. We have used unpublished measurements at SLAC of the inclusive charged pion yield (integrated over the bremsstrahlung flux) to estimate the inclusive photon production yield from the decay of neutral pions. Our resulting estimates are in agreement with the inclusive photon data of Ref. 14. The mean energy from π^0 decay photons summed over four calorimeter blocks and integrated over 30 ns is always less than 10% of the Compton energy. However, contrary to the atomic Compton case, this pile-up is typically 1 or 2 photons. Thus the poisson fluctuations are important. We have calculated the probability that the poisson fluctuations yield a pile-up energy summed over four calorimeter blocks exceeding 30% of the Compton energy, when integrated over any random 30ns ADC gate. The result we denote by P_{30} . The solid angle of four calorimeter blocks we denote by $\Delta\Omega_4$. We also assume that with a TDC on each calorimeter block, we can do proton-photon coincidence timing to a precision of 5 ns (full width), thus effectively dividing the ADC gate into 6 intervals. For a given proton, 63% of the true Compton coincidences lie with the 1σ solid angle $\pi\sigma_\theta\sigma_\phi$. Thus the contribution to the Compton signal to noise ratio from accidental coincidences is

$$\frac{S[p(\gamma, \gamma p)]}{N[p(\gamma, \gamma')X]} = \frac{d\sigma(\gamma, p\gamma)}{d\sigma(\gamma, p)X} \frac{63\%}{(\pi\sigma_\theta\sigma_\phi)} \bigg/ \frac{(P_{30}/6)}{\Delta\Omega_4}. \quad (2.16)$$

These results are tabulated in column 5 of Table 2. The net signal to background for Compton photons is the sum in parallel (the inverse of the sum of the inverses) of columns 4 and 5 of Table 2.

The leading photons from exclusive π^0 production must also be separated from the random coincidence background. One half of the leading photons lie within a solid angle $\pi(m_\pi/k')^2/3$ that is one third of the total angular spread of the π^0 decay photons. Thus the signal to noise ratio for the leading photons

from exclusive π^0 production is

$$\frac{S(\gamma, p\gamma_1)\gamma_2}{N(\gamma, \gamma')X} = \frac{d\sigma(\gamma, p)\pi^0}{d\sigma(\gamma, p)X} \frac{3/2}{\pi(m_\pi/k')^2} \Big/ \frac{P_{30}/6}{\Delta\Omega_4}. \quad (2.17)$$

These results are tabulated in column 6 of Table 2. Although the exclusive pion rate is much greater than the Compton rate, the photons from exclusive pion production are spread out over a much larger solid angle.

2.6 CALIBRATION

For both the Compton and π^0 reactions, it is very important to accurately calibrate the angular placement of the calorimeter. There is a natural calibration measurement for the coincidence kinematics. We will use the electron beam to measure elastic $p(e, ep)$ scattering. The kinematics are identical to the endpoint kinematics of $p(\gamma, \gamma p)$. The dominant backgrounds in the End Station from the electron beam will be deep inelastic scattering and the inclusive yield induced by bremsstrahlung in the target. Thus if the electron current on the target during the calibration runs is 1 - 5 mA peak (and if the beam is cleanly dumped) then the background with the electron beam will be no worse than with the photon beam.

2.7 RUN PLAN

We assume one 8 hour shift of downtime to move the calorimeter, and 4 hours of downtime to change beam energies. At each calorimeter angle, we will scan through the desired energies. We base our run time estimates on a desire for 200 counts in the Compton peak, but not less than 4 hours and not more than 100 hours at each point. We note that 50 counts in the Compton peak with a 1:1 signal to noise ratio is a 20% statistical measure. We include a 20% overhead for $p(e, e'p)$ calibration measurements and a 10% overhead for target empty runs. With a total of 5 angle changes and 19 energy changes, we anticipate downtime of $5 \cdot 8 \text{ hr} + 19 \cdot 4 \text{ hr} = 116 \text{ hr}$. The run time is summarized below:

$k(\text{GeV})$	Hours
4.0	12
6.0	50
8.8	160
12.9	180
Subtotal	402
$p(e, e'p)$	80
Target Empty	40
Angle & Energy changes	116
Total	640

Assuming a 65% overall efficiency, we request a 6 calendar week run.

2.8 CONCLUSION

Elastic scattering from the proton is one of the experiments for which SLAC was built. Culminating 25 years of heroic work, the unseparated cross sections have been measured to $Q^2 = 32 (\text{GeV}/c)^2$ (Ref.16) and the longitudinal and transverse cross sections have been separated for $Q^2 \leq 9 (\text{GeV}/c)^2$ (Ref. 17). In just 6 weeks, we can measure the elastic Compton cross section to $s = 23 \text{ GeV}^2$ and $|t| \leq 13 (\text{GeV}/c)^2$. Within the foreseeable future, these experiments are only possible at SLAC.

The contrast of Fig. 10 with Fig. 2 & 3 illustrates that Compton scattering is more sensitive to details of the proton distribution amplitude than elastic electron scattering. Once the scaling regime is reached ($Q^2 > 5 (\text{GeV}/c)^2$), the pQCD prediction for the elastic form factor is *a single number* (aside from the $\ln Q^2$ evolution), whereas for Compton scattering, the pQCD prediction is an angular distribution. Fig. 10 includes the pQCD predictions based on three of the same QCD sum-rule proton distribution amplitudes as in Fig. 2.

APPENDIX A

Kinematics

Our choice of kinematics is listed in Table 1. These kinematics were chosen to optimize several criteria. First, we start at $k = 4.0$ GeV to overlap the points of Ref. 9. This requires only modest beam time. Second, we wish to cover the widest possible range in s , particularly at $\theta_{CM} = \pi/2$, where both u and t are large. Third, at fixed s , we wish to measure the angular distribution over the widest possible range. Finally, we need to minimize the number of angle changes for the calorimeter in order to most efficiently use the beam time. Fortunately, nearly all of these criteria can be met simultaneously if we choose endpoint energies such that the values of s form a geometric series. This has the added virtue that points of equal statistical error-bar contribute equally to the precision of the power law S^α fit if the kinematics are a geometric series in s .

With $s^{(n)} = \alpha^n s_0$, we select our kinematics by first requiring $\theta_{CM} = \pi/2$ for each value of s . This results in laboratory scattering angles of

$$\cos \theta_{\text{lab}}^{(n)} = \beta^{(n)} = \frac{k^{(n)}}{k^{(n)} + M} = \frac{s^{(n)} - M^2}{s^{(n)} + M^2}. \quad (\text{A1})$$

Using the lab angles $\theta_{\text{lab}}^{(m)}$ at each photon energy defined by $s^{(n)}$ results in CM scattering angles given by

$$\cos \theta_{CM} = \frac{\beta^{(n)} - \cos \theta_{\text{lab}}^{(m)}}{1 - \beta^{(n)} \cos \theta_{\text{lab}}^{(m)}} = \frac{\alpha^{(n-m)} - 1}{\alpha^{(n-m)} + 1}, \quad n - m = 0, \pm 1, \pm 2, \dots \quad (\text{A2})$$

We choose $\alpha^3 = 3$ such that our kinematics includes $\cos \theta_{CM} = 0.0$ and 0.5 . Also, the scaling law S^{-6} falls by a factor of 9 for each step in s .

APPENDIX B

Contributions to Photon Angular Resolution

Compton events and exclusive π^0 events are identified by a coincidence between the proton and photon arms. Compton, exclusive π^0 and inclusive γ -rays are distinguished by the distributions of $\delta\theta_\gamma$ and $\delta\phi_\gamma$: the difference, respectively, of the measured in-plane and out-of-plane photon angles with respect to the Compton photon angles determined by the proton kinematics measured in the 8 GeV spectrometer. Thus the resolution in $\delta\phi_\gamma$ has contributions added in quadrature from:

1. The calorimeter position resolution;
2. The vertical beam spot size;
3. The proton multiple scattering in the target; and
4. The proton vertical angle resolution.

Similarly, the resolution in $\delta\theta_\gamma$ has contributions from

1. The calorimeter position resolution;
2. The horizontal beam spot size;
3. The proton vertex resolution along the beam line;
4. The proton multiple scattering in the target;
5. The proton scattering angle resolution; and
6. The proton momentum resolution.

The first order matrix elements (for $p_p \leq 4.5$ GeV) of the 8 GeV Spectrometer optics in the large acceptance tune are listed in Table 3. Coordinates with a subscript 0 are variables at the target. Unsubscripted coordinates are the variables at the spectrometer focal plane. $\sigma(x_0)$ is the vertical r.m.s. beam spot size defined by the collimators and $\sigma_z = \sigma(y_0)/\sin\theta_p$ is the vertex resolution along the beam axis. We assume that the Calorimeter will localize the shower to a spatial precision of 2 cm (σ). We assume an r.m.s beam spot on target of $\sigma(\text{spot}) = 1$ cm, corresponding to a uniform disk of radius 1.25 cm defined by the photon beam collimation.

Assuming a 2.5 cm radius target cell and 0.1 g/cm² Al walls, the multiple scattering (polar-) angle is

$$\sigma(\text{Multiple Scattering}) = \frac{16 \text{ MeV}}{p_p} \sqrt{\frac{0.007}{\sin\theta_p}} \quad (\text{B1})$$

The contribution to $\sigma(\theta_\gamma)$ from the proton arm measurement of the vertex along

the target length is

$$\sigma(\theta_\gamma) = \frac{\sigma(y_0) \sin \theta_\gamma}{r_{EM} \sin \theta_p}, \quad (\text{B2})$$

where r_{EM} is defined in Eq. (2.5). The contribution to $\sigma(\theta_\gamma)$ from the beam spot size is

$$\sigma(\theta_\gamma) = \frac{\sigma(\text{spot})}{r_{EM}} \left[\cos \theta_\gamma + \frac{\sin \theta_\gamma}{\sin \theta_p} \cos \theta_p \right] \quad (\text{B3})$$

The resolution in θ_γ derived from the precision of the proton measurements of θ_p and p_p is:

$$\sigma(\theta_\gamma) \sin \theta_\gamma = \left[\frac{\partial \cos \theta_\gamma}{\partial \cos \theta_p} \Big|_{p_p} \sin(\theta_p) \sigma(\theta_p) \oplus \frac{\partial \cos \theta_\gamma}{\partial p_p} \Big|_{\cos \theta_p} \sigma(\delta) p_p \right], \quad (\text{B4})$$

where \oplus denotes addition in quadrature. Similarly, the calorimeter acceptance in the horizontal plane, required to match the proton acceptance, is defined by the coherent sum the contributions from the proton angular acceptance $\Delta\theta_p$ and the proton momentum acceptance Δp_p :

$$\Delta\theta_\gamma = \left[\frac{\partial \cos \theta_\gamma}{\partial \cos \theta_p} \Big|_{p_p} \sin \theta_p \Delta\theta_p + \frac{\partial \cos \theta_\gamma}{\partial p_p} \Big|_{\cos \theta_p} \Delta p_p \right] / \sin \theta_\gamma \quad (\text{B5})$$

The sum of all the contributions to the angular resolution are listed in Table 2 as a function of the kinematics. The vertical angle resolution is dominated by the 8 GeV vertical angle resolution. The horizontal angular resolution is made up in varying degrees by the longitudinal vertex resolution (as measured by the 8 GeV spectrometer), the proton recoil momentum resolution (limited by the vertical spot size) and the horizontal spot size.

Table. 1							
$p(\gamma, \gamma'p)$ Kinematics and Count Rate							
Electron Flux = 50. mA peak in 1.6 μ sec pulse width at 120. Hz							
$\Phi_\gamma/X_{\text{eff}} = 5.0 \cdot 10^9$ Equivalent quanta per burst per percent radiation length							
$\mathcal{L}_\gamma/X_{\text{eff}} = 6.0 \cdot 10^3$ Counts per burst per μ b per percent radiation length							
θ_{CM} (deg)	$-t$ (GeV/c) ²	k' (GeV)	θ_{lab} (deg)	p_P (GeV/c)	θ_P (deg)	$p(\gamma, p)\gamma$ (Hour ⁻¹)	$p(\gamma, p)\pi^0$ (Hour ⁻¹)
$k = 4.0$ GeV		$S = 8.4$ GeV ²					
$X_{\text{eff}} = 0.22\%$							
43.6	0.9	3.5	14.8	1.1	55.7	205.0	9770.
60.0	1.7	3.1	21.2	1.6	45.4	50.1	2360.
90.0	3.4	2.2	35.9	2.6	30.4	22.9	979.
$k = 6.0$ GeV		$S = 12.1$ GeV ²					
$X_{\text{eff}} = 0.48\%$							
51.4	2.0	4.9	14.8	1.7	46.3	42.0	1383.
60.0	2.6	4.6	17.7	2.1	41.1	21.9	715.
69.5	3.4	4.2	21.2	2.6	36.0	13.5	430.
79.6	4.3	3.7	25.3	3.1	31.1	10.5	323.
90.0	5.2	3.2	30.2	3.6	26.7	10.3	306.
100.4	6.1	2.7	35.9	4.1	22.7	11.8	341.
$k = 8.8$ GeV		$S = 17.4$ GeV ²					
$X_{\text{eff}} = 0.99\%$							
60.0	3.9	6.7	14.8	2.9	36.5	9.2	208.
69.5	5.1	6.1	17.7	3.5	31.7	5.8	127.
79.6	6.4	5.4	21.2	4.3	27.2	4.5	97.
90.0	7.9	4.6	25.3	5.0	23.2	3.6	74.
100.4	9.3	3.9	30.2	5.8	19.6	3.1	63.
110.5	10.6	3.2	35.9	6.5	16.5	3.0	59.
$k = 12.9$ GeV		$S = 25.2$ GeV ²					
$X_{\text{eff}} = 1.93\%$							
69.5	7.6	8.9	14.8	4.9	27.5	2.0	30.
79.6	9.6	7.8	17.7	6.0	23.5	1.1	16.
90.0	11.7	6.7	21.2	7.1	19.9	0.8	11.
100.4	13.8	5.6	25.3	8.3	16.7	0.7	9.

Table. 2					
$p(\gamma, \gamma'p)$ Angular Resolution					
1	2	3	4	5	6
θ_{CM} (deg)	$\sigma(\phi_\gamma)$ mrad	$\sigma(\theta_\gamma)$ mrad	$\frac{S[p(\gamma, \gamma)p]}{N[p(\gamma, \pi^0)p]}$	$\frac{S[p(\gamma, \gamma)p]}{N[p(\gamma, \gamma')X]}$	$\frac{S[p(\gamma, \pi^0)p]}{N[p(\gamma, \gamma')X]}$
$k = 4.0$ GeV		$S = 8.4$ GeV ²			
43.63	1.05	1.76	3.41	14.25	3.14
60.00	1.64	2.03	2.44	13.16	4.05
90.00	3.78	3.58	1.31	4.44	2.54
$k = 6.0$ GeV		$S = 12.1$ GeV ²			
51.35	1.13	1.34	3.04	8.90	2.20
60.00	1.44	1.42	2.62	8.08	2.31
69.47	1.88	1.55	2.27	7.72	2.55
79.57	2.50	1.83	1.90	7.20	2.83
90.00	3.37	2.48	1.45	3.86	2.00
100.43	4.61	3.95	0.96	1.58	1.23
$k = 8.8$ GeV		$S = 17.4$ GeV ²			
60.00	1.30	1.00	2.78	7.79	2.10
69.47	1.71	1.11	2.37	4.37	1.39
79.57	2.31	1.32	1.95	4.88	1.88
90.00	3.14	1.79	1.49	2.28	1.15
100.43	4.32	2.78	1.02	1.02	0.75
110.53	5.95	4.88	0.65	0.41	0.47
$k = 12.9$ GeV		$S = 25.2$ GeV ²			
69.47	1.60	0.82	2.33	3.44	1.11
79.57	2.18	1.00	1.87	2.14	0.86
90.00	3.00	1.36	1.42	1.37	0.72
100.43	4.16	2.06	1.01	0.73	0.54

Table 3: 8 GeV First Order Optics			
Vertical plane		Horizontal plane	
$\langle x x_0 \rangle =$	-2.64	$\langle y y_0 \rangle =$	0.0
$\langle x \phi_0 \rangle =$	0.0	$\langle y \theta_0 \rangle =$	1.13 cm/mr
$\langle \phi x_0 \rangle =$	8.7 mr/cm	$\langle \theta y_0 \rangle =$	-0.88 mr/cm
$\langle \phi \phi_0 \rangle =$	-0.37	$\langle \theta \theta_0 \rangle =$	0.969
$\langle x \delta \rangle =$	2.5 cm/%	$\langle y \delta \rangle =$	0.0
$\langle \phi \delta \rangle =$	-0.89 mrad/%	$\langle \theta \delta \rangle =$	0.0
Measurement Resolution at Focal Plane			
$\sigma(x) =$	0.1 cm	$\sigma(y) =$	0.2 cm
$\sigma(\phi) =$	1.0 mr	$\sigma(\theta) =$	2.0 mr
Beam spot			
$\sigma(x_0) =$	1.0 cm		
Measurement Resolution at Target			
$\sigma(\delta) = \sigma(x_0) \langle x x_0 \rangle / \langle x \delta \rangle$		$\sigma(y_0) = \frac{\sigma(\theta_p)}{\langle \theta y_0 \rangle} \oplus \frac{\sigma(y) \langle \theta \theta_0 \rangle}{\langle y \theta_0 \rangle \langle \theta y_0 \rangle}$	
	= 1%		= 2.3 cm
$\sigma(\phi_p) = \sigma(\phi) / \langle \phi \phi_0 \rangle$		$\sigma(\theta_p) = \sigma(y) / \langle y \theta_0 \rangle$	
	= 2.7 mr		= 0.2 mr

REFERENCES

1. F.J. Federspiel, *et al.*, Phys Rev Lett **67** 1511 (1991).
2. Marc Damashek and Frederick J. Gilman, Phys Rev **D1** 1319 (1970).
3. L. Frankfurt, G.A. Miller, and M. Strikman, submitted for publication, March 1992, and references therein.
4. Stanley J. Brodsky and Glennys R. Farrar, Phys Rev Lett, **31** 1153 (1973).
5. R.L. Anderson, *et al.*, Phys Rev Lett, **25** 1218 (1970).
6. A.M. Boyarski, *et al.*, Phys Rev Lett, **26** 1600 (1971).
7. M. Deutsch, *et al.*, Phys Rev **D11** 3828 (1973).
8. J. Duda, *et al.*, Z Phys **C17** 319 (1983).
9. M.A. Shupe, *et al.*, Phys Rev **D19** 1921 (1979).
10. A.M. Breakstone, *et al.*, Phys Rev Lett **47** 1778 (1981).
11. Glennys R. Farrar and Huayi Zhang, Phys Rev **D41** 3348 (1990).
12. A.S. Kronfeld and B. Nizic, Phys Rev **D44** 3445 (1991).
13. R.L. Anderson, Nucl Inst Meth, **65** (1968) 195.
14. A.M. Eisner, *et al.*, PRL **33** (1974) 865, and
D.O. Caldwell, *et al.*, *ibid.*, 868.
15. R. Anderson, *et al.*, Phys Rev **D1** (1970) 27.
16. R.G. Arnold, *et al.*, Phys Rev Lett **57** (1986) 174.
17. P.E. Bosted, *et al.*, Phys Rev Lett, **68** (1992) 3841.
18. Paul Stoler, Nucl Phys **A532** 377c (1991).

FIGURE CAPTIONS

1. A compilation of high energy $p(\gamma, \gamma')p$ data.^{5,6,7,8,9} The data are displayed as $s^6 d\sigma/dt$ vs. $\cos\theta_{CM}$ in order to test the pQCD scaling law of Eq. (1.1). Not shown are the data of Ref. 10, which integrate over wide bins in s .
2. The world's supply of $p(\gamma, \gamma')p$ data for $|t| > 1.0$ (GeV/c)² (Ref. 9). The curves are the pQCD calculations discussed in the text.
3. Dimensional counting scaling law behavior of $p(\gamma, \gamma p)$. The points with error bars are the data of Ref. 9. The solid lines are the one-sigma error band of a $s^{-\alpha} f_{\gamma}(\theta_{CM})$ fit to the data at each CM angle. Note the wide divergence of the error bands at kinematics of our proposed points. The dashed, dotted, and dot dashed lines are the pQCD calculations of Ref. 12, using the proton distributions COZ, KS, and GS, respectively. The solid boxes are the expected results from this proposal. The vertical size of the box represents a one-sigma error-band. The horizontal size represents the photon energy acceptance. a) 60°; b) Data at 65° and 75°, proposed points at 70° and 80°; c) 90°; d) Data and theories at 105°, proposed points at 100° and 110°.
4. $p(\gamma, \pi^0)p$ data, same reference as Fig.2.
5. Four versions of the proton distribution amplitude, as tabulated in Ref. 12.
6. Kinematics of proposed $p(\gamma, \gamma'p)$ and $p(\gamma, \pi^0p)$ measurements, in the t vs s plane. The squares are the proposed points. The crosses are the kinematics of Ref. Shupe. The solid lines are contours of constant θ_{CM} .
7. Proposed coincidence kinematics in the θ_p vs θ_{γ} plane. The solid lines are contours of constant θ_{CM} . The dashed lines are contours of constant incident energy.
8. Layout of Calorimeter and 8 GeV spectrometer in ESA. The black squares are the six calorimeter positions along a spiral track, defined in the text. The squares are to scale, not including the concrete shielding.
9. Coplanarity distribution from Ref. 9 at $k = 3$ GeV and $t = -0.71$ GeV². (a) without and (b) with a cut on $\Delta\theta$ (the in-plane angle).
10. Elastic Magnetic form factor of the proton.¹⁸ The curves at high Q^2 correspond to three of the same pQCD calculations discussed for Compton scattering. The slopes of the curves are indicative of the expected QCD evolution with Q^2 .

$$\gamma + p \longrightarrow \gamma + p$$

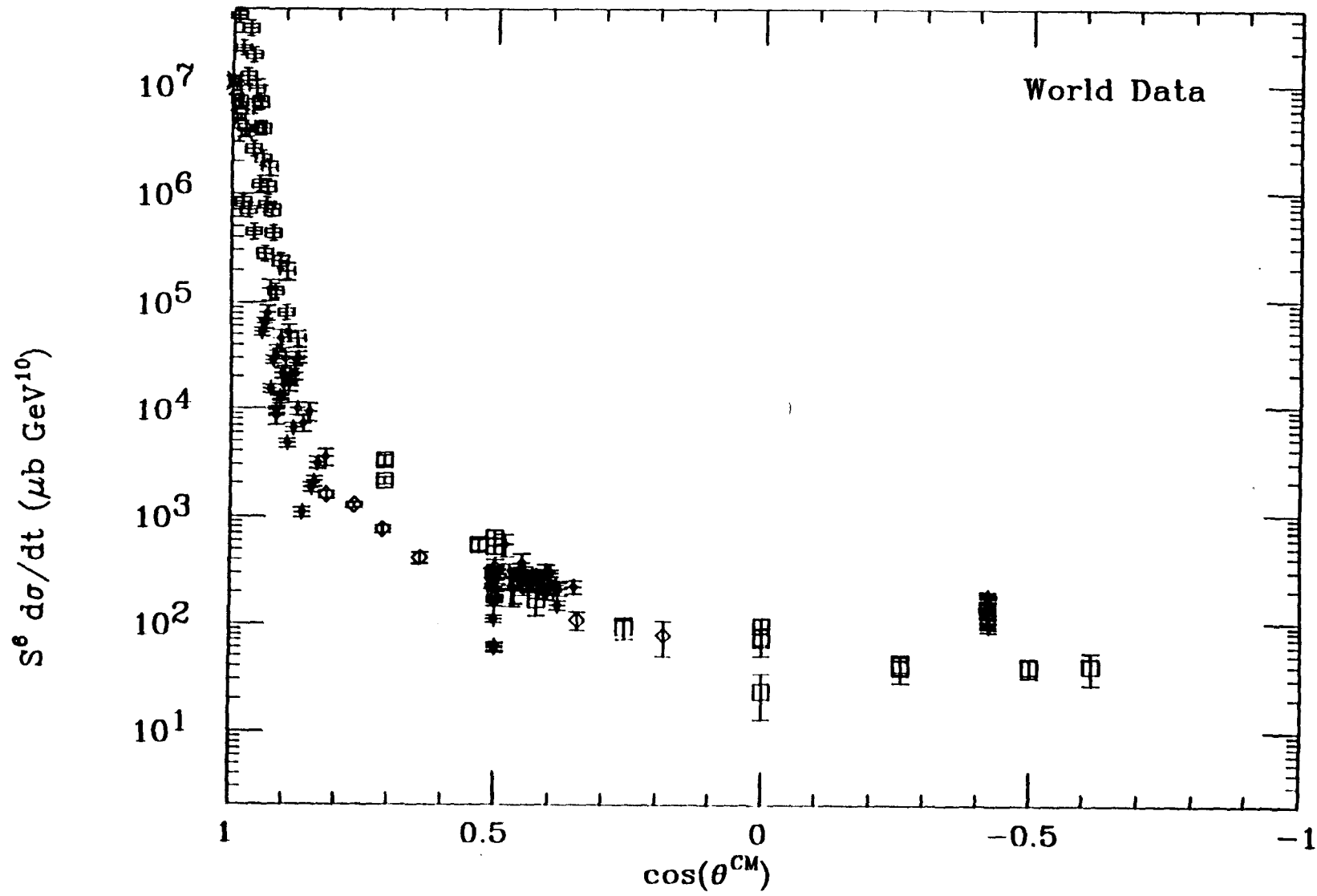


Fig. 1

Fig. 2

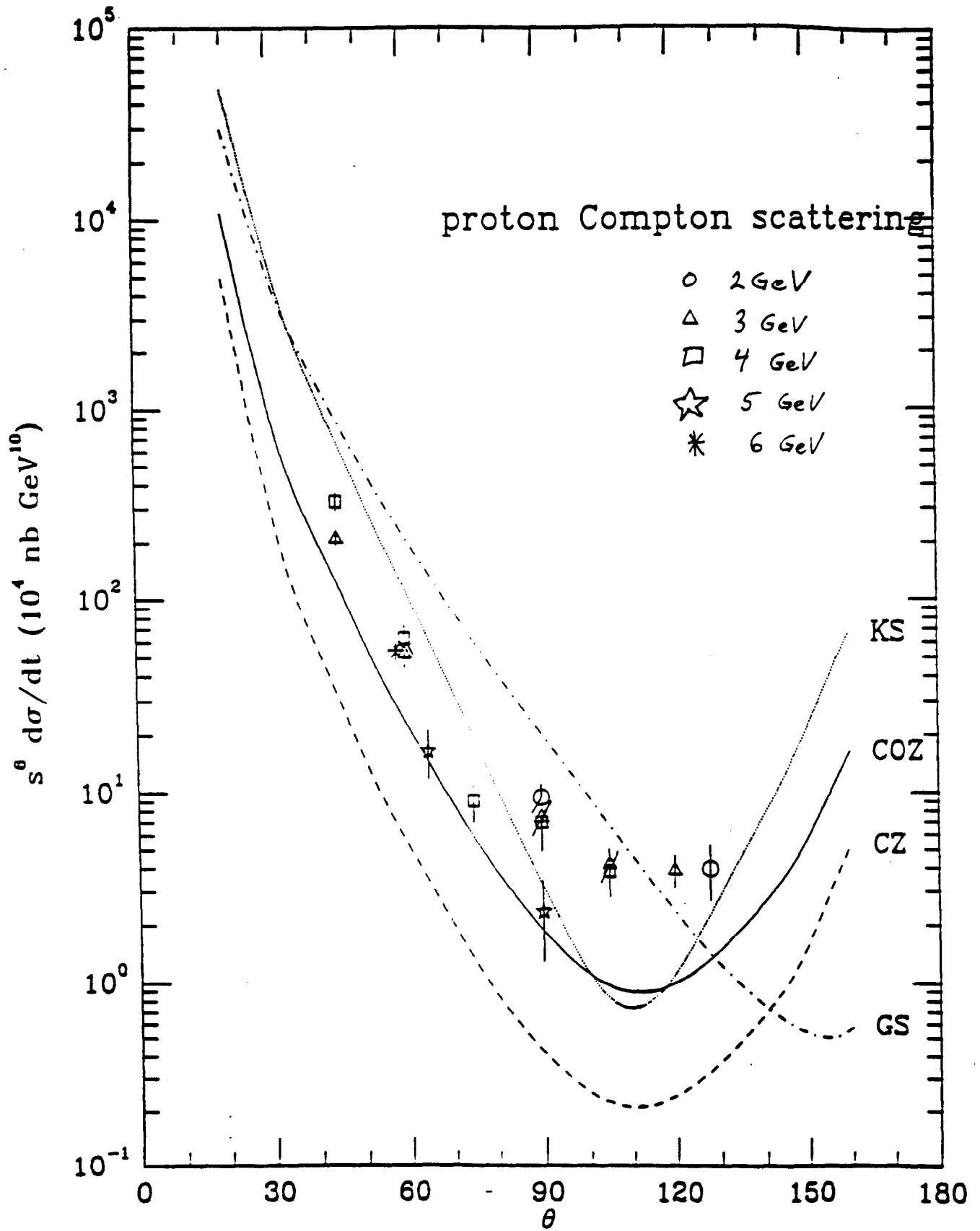
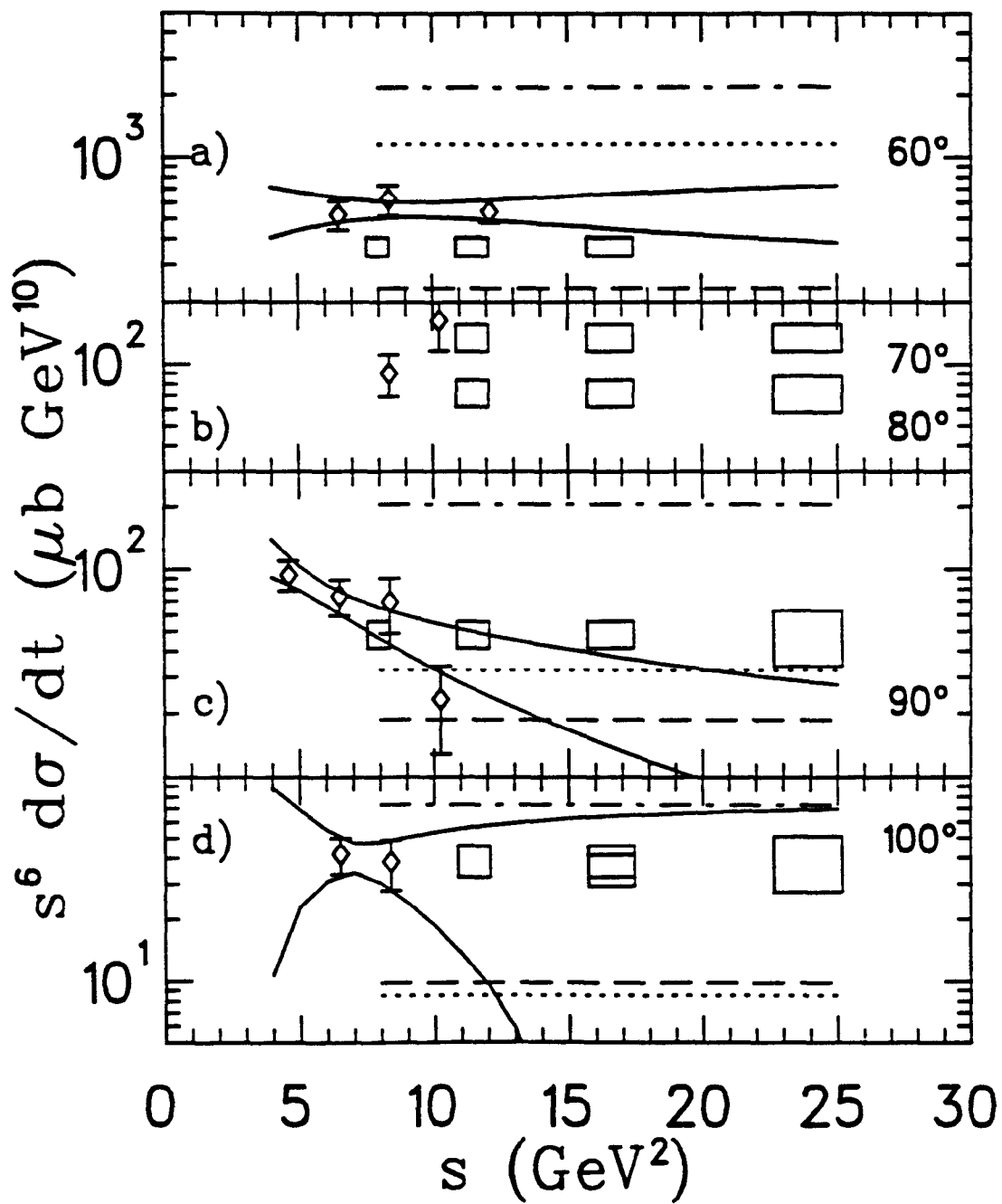


Fig. 3 $p(\gamma, \gamma p)$



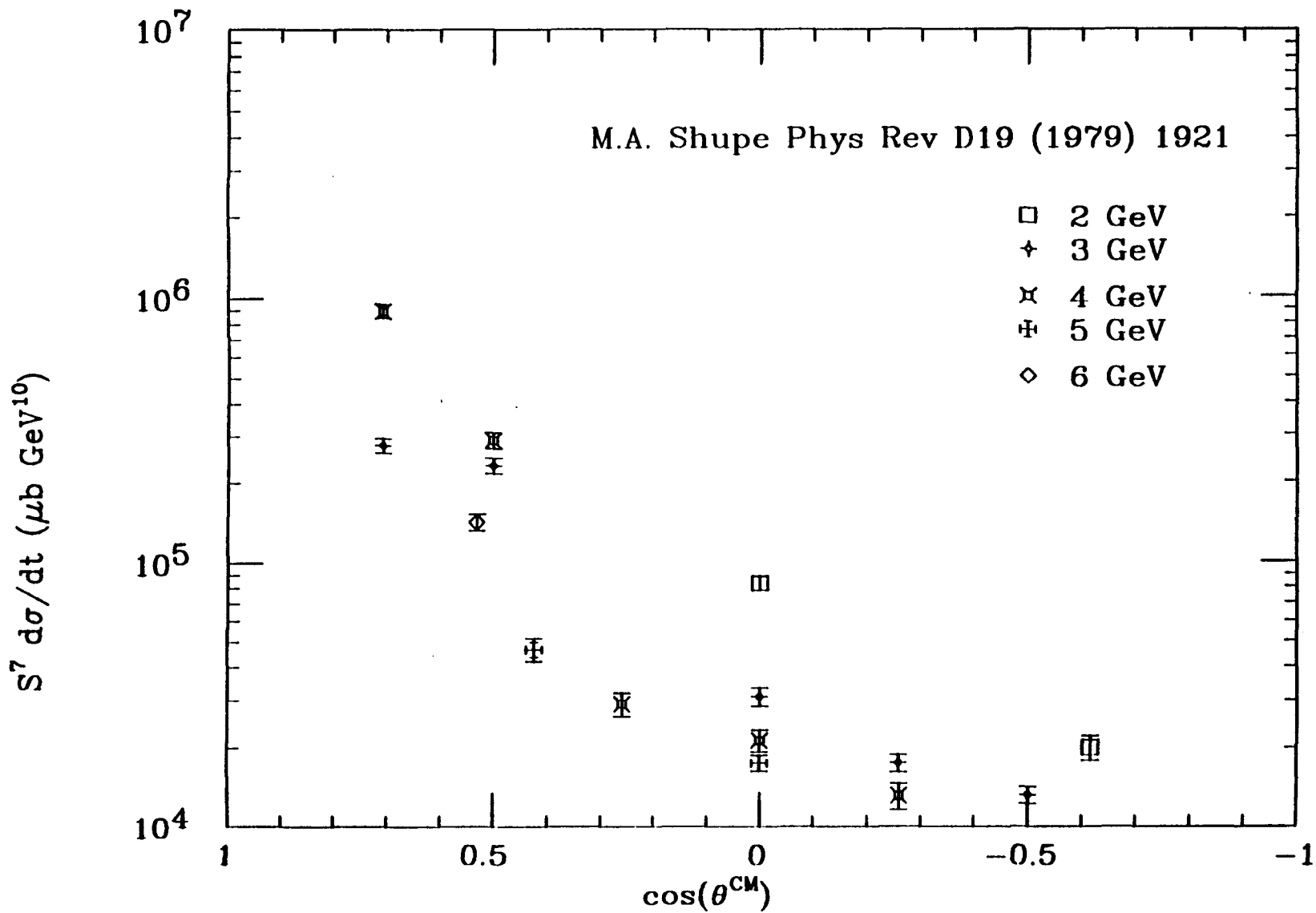
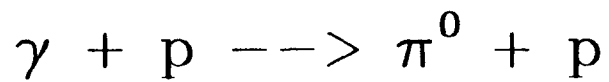
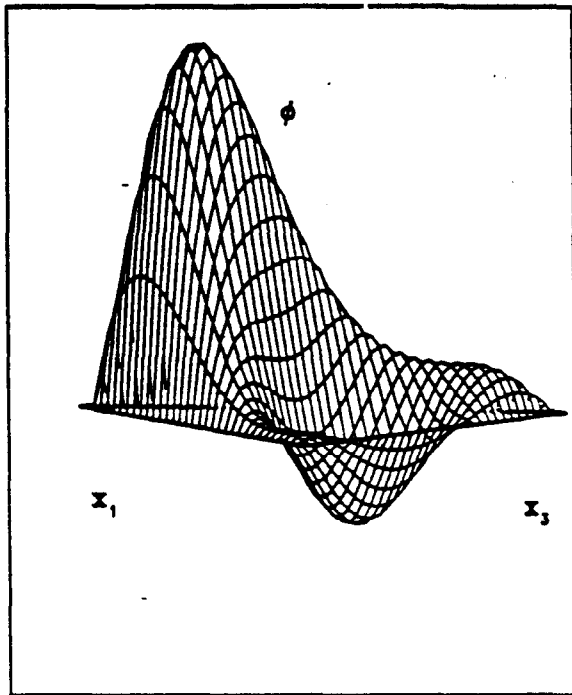
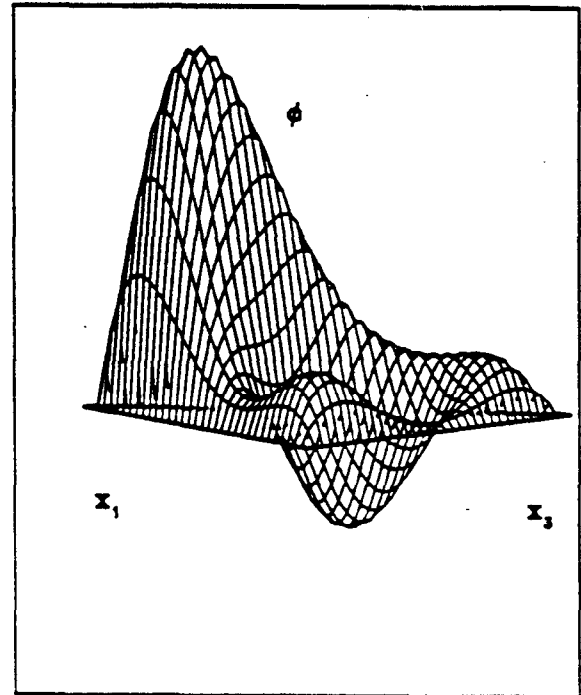


Fig. 4

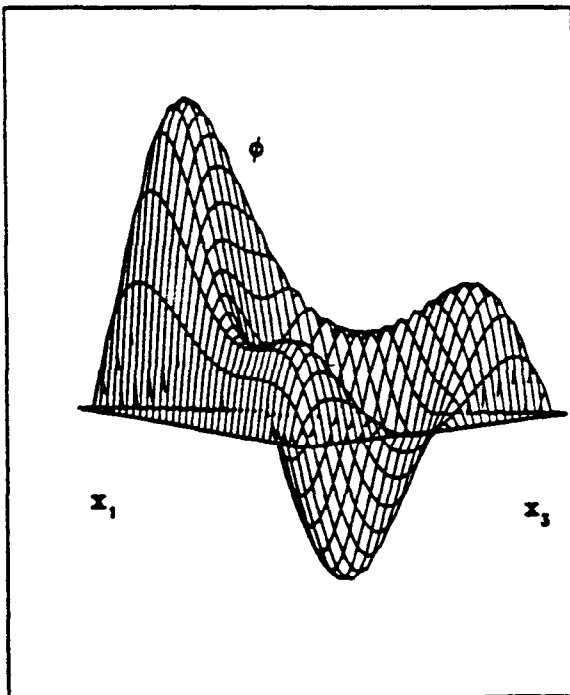
Fig. 5
Proton Distribution Amplitude



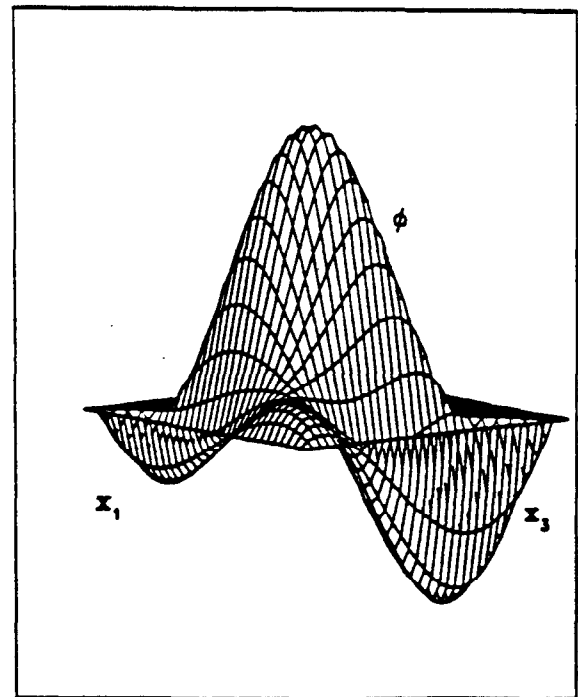
CZ



COZ



KS



GS

Fig. 6 $p(\gamma,\gamma)p$ Kinematics

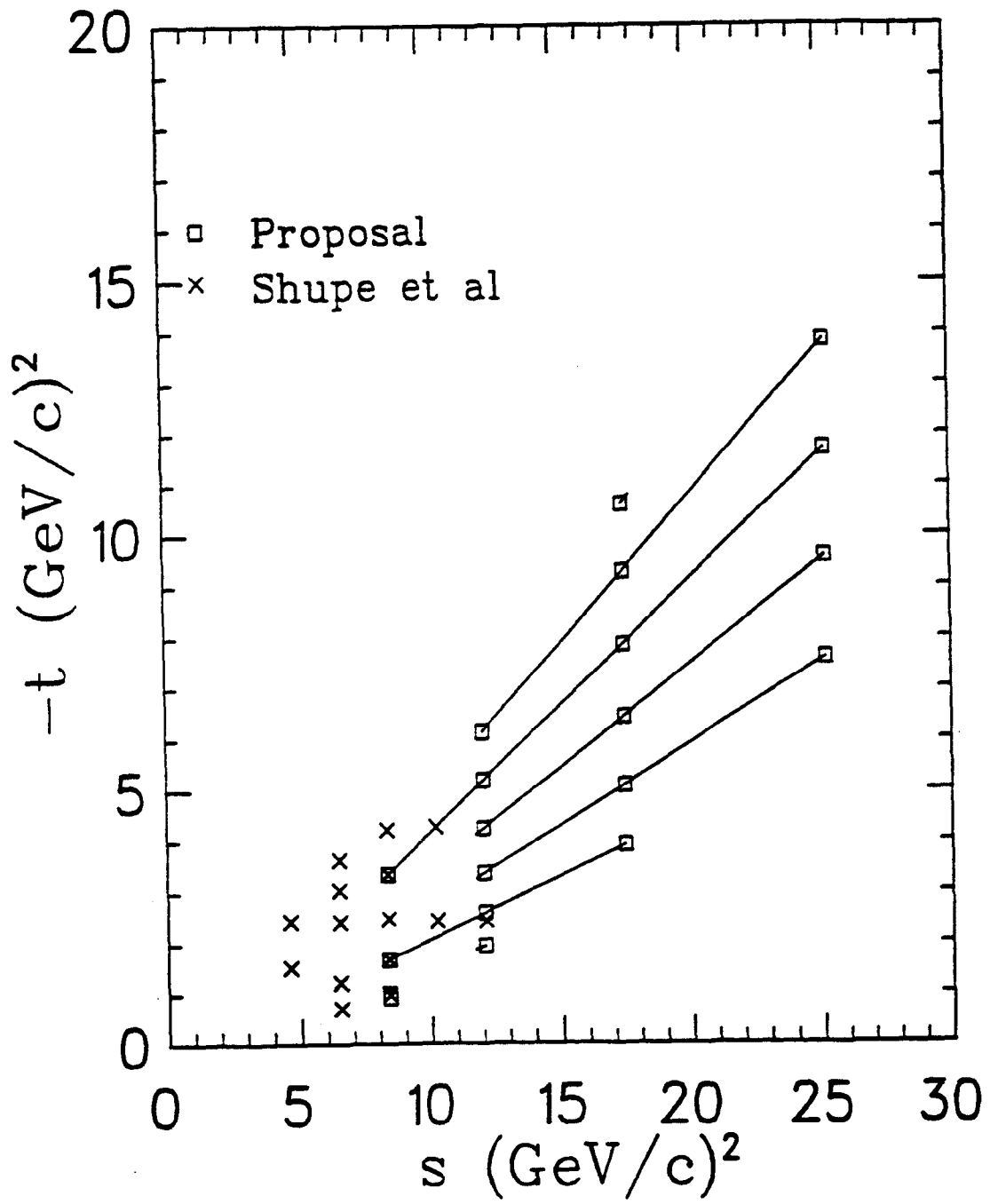
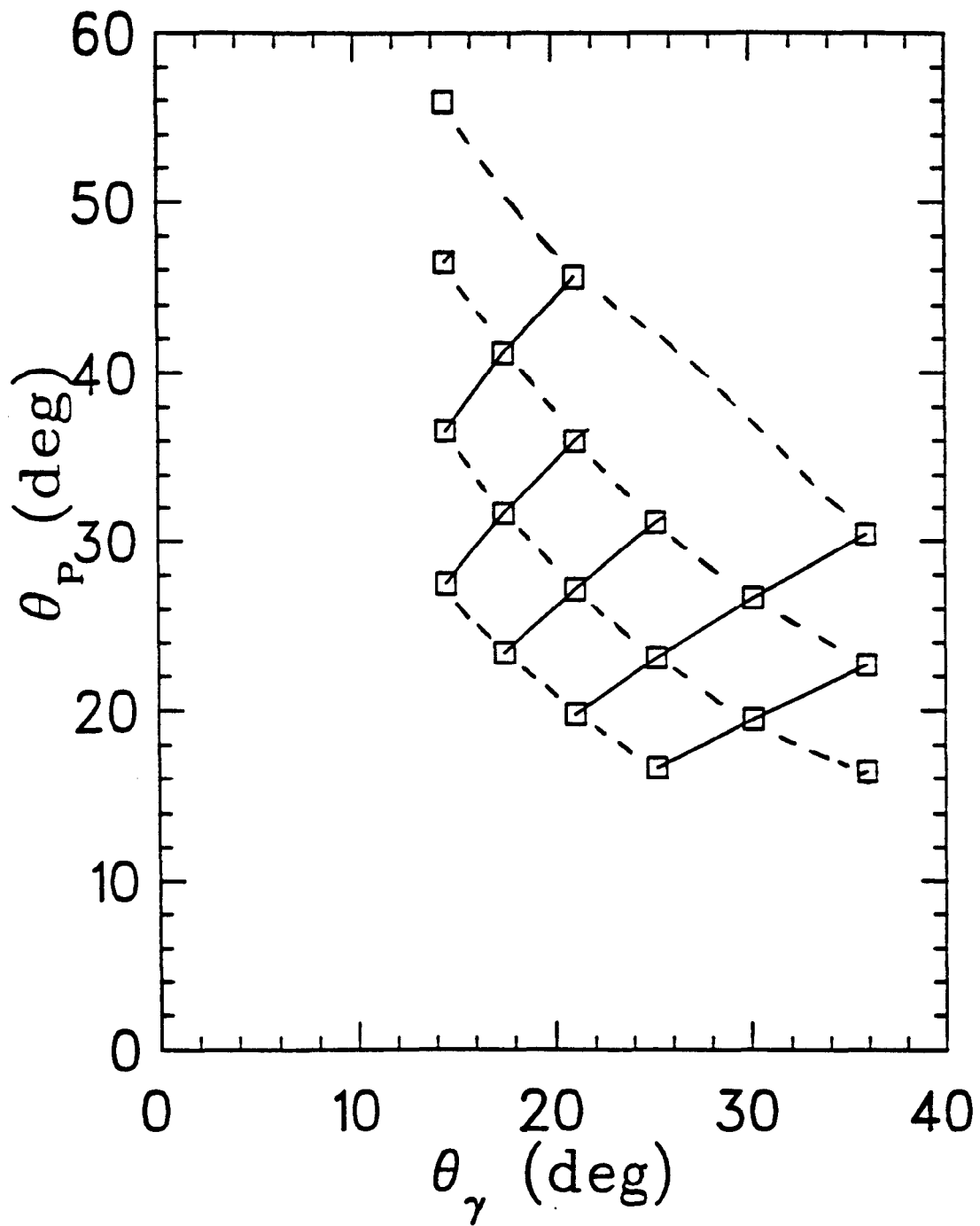


Fig. 7 $p(\gamma,\gamma)p$ Kinematics



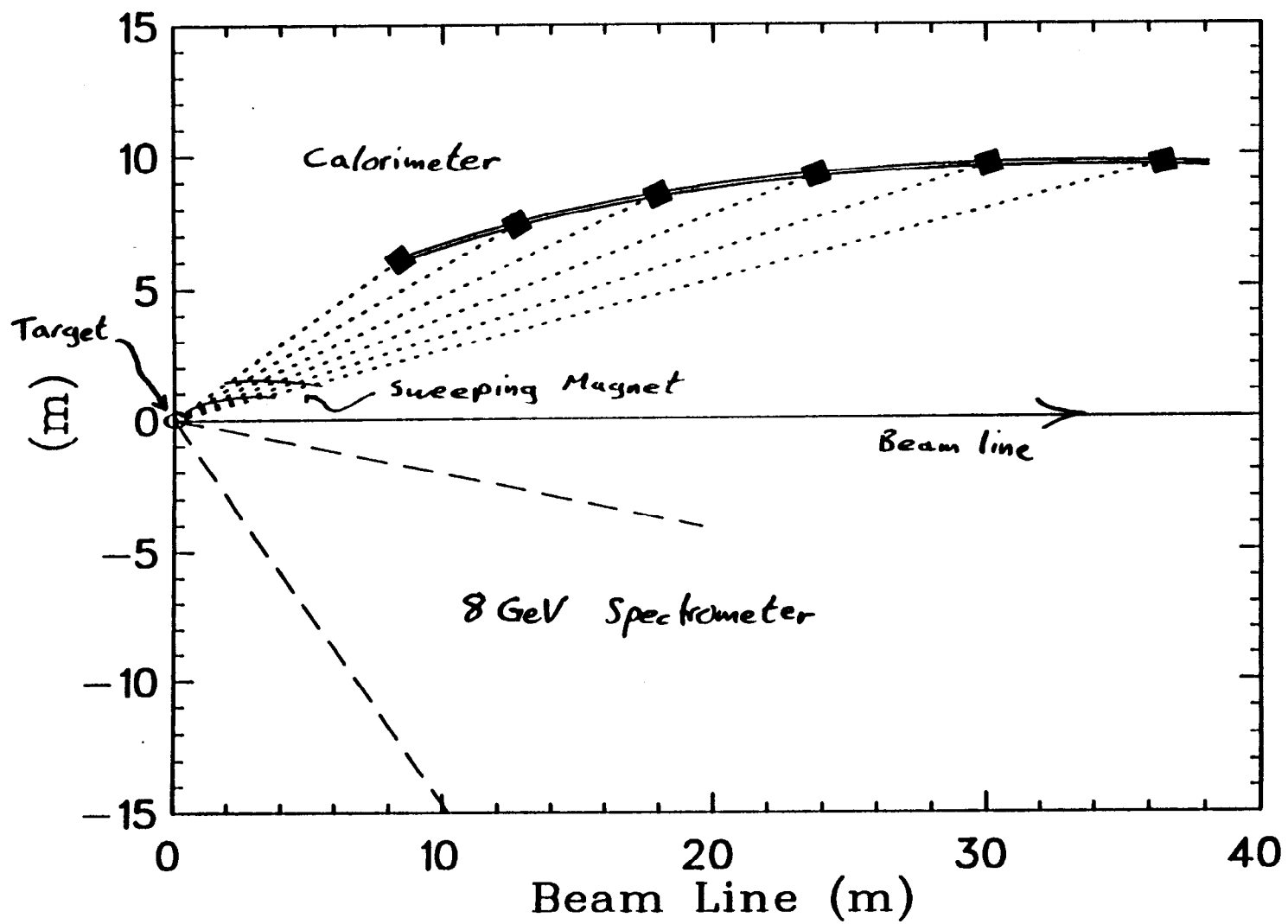


Fig. 8 ESA Floor Plan

Fig. 9 $p(\gamma, \gamma' p)$
Coincidence Angular Correlation

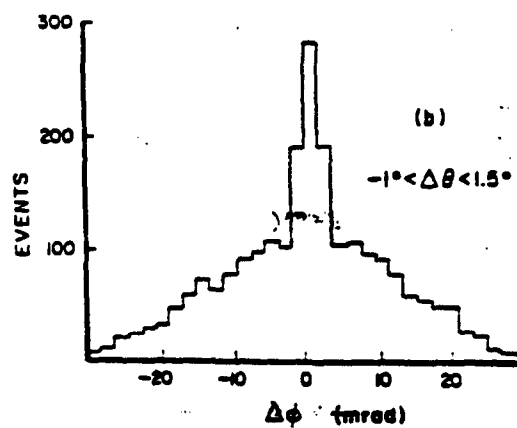
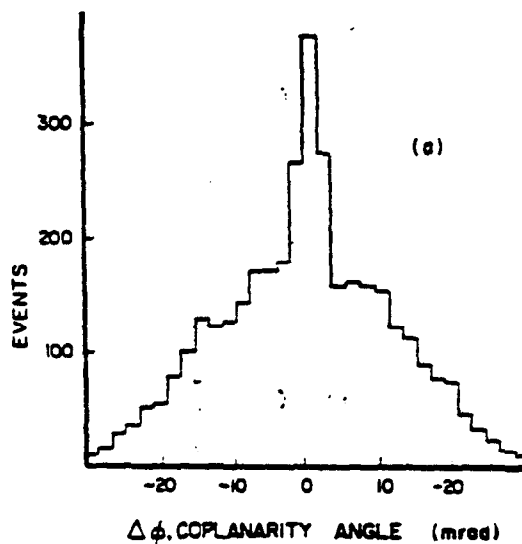


FIG. 2. Coplanarity distributions at 3 GeV and $s=0.71$ GeV^2 . (a) without and (b) with a cut on the $\Delta\theta$.

Fig. 10 $p(e,e)p$

